coatings

MDPI

Article

Tunable Microstructure and Morphology of the Self-Assembly Hydroxyapatite Coatings on ZK60 Magnesium Alloy Substrates Using Hydrothermal Methods

Taolei Wang [1], Chao Lin [2], Dan Batalu [3], Jingzhou Hu [2] and Wei Lu [1,*]

[1] Shanghai Key Laboratory of D&A for Metal-Functional Materials, School of Materials Science and Engineering, Tongji University, Shanghai 201804, China; wangtaolei@tongji.edu.cn
[2] Department of Oral and Maxillofacial-Head and Neck Oncology, Ninth People's Hospital, Shanghai Jiao Tong University School of Medicine, Shanghai 200011, China; fyfanxin@wfmc.edu.cn (C.L.); huyayi@shsmu.edu.cn (J.H.)
[3] Faculty of Material Science and Engineering, University Politehnica of Bucharest, Splaiul Independentei 313, 011061 Bucharest, Romania; dan_batalu@yahoo.com
* Correspondence: weilu@tongji.edu.cn

Abstract: Hydroxyapatite coatings have been widely used to improve the corrosion resistance of biodegradable magnesium alloys. In this paper, in order to manufacture the ideal hydroxyapatite (HA) coating on the ZK60 magnesium substrate by hydrothermal method, formation mechanism of enhanced hydroxyapatite (HA) coatings, influence of pH values of the precursor solution on the HA morphology, corrosion resistance and cytotoxicity of HA coatings have been investigated. Results show that the growth pattern of the HA is influenced by the local pH value. HA has a preferential c-axis and higher crystallinity in the alkaline environment developing a nanorod-like structure, while in acid and neutral environments it has a preferential growth along the a(b)-plane with a lower crystallinity, developing a nanosheet-like structure. The different morphology and microstructure lead to different degradation behavior and performance of HA coatings. Immersion and electrochemical tests show that the neutral environment promote formation of HA coatings with high corrosion resistance. The cell culture experiments confirm that the enhanced corrosion resistance assure the biocompatibility of the substrate-coating system. In general, the HA coating prepared in neutral environment shows great potential in surface modification of magnesium alloys.

Keywords: hydroxyapatite; grain growth; corrosion resistance; biomedical applications

Citation: Wang, T.; Lin, C.; Batalu, D.; Hu, J.; Lu, W. Tunable Microstructure and Morphology of the Self-Assembly Hydroxyapatite Coatings on ZK60 Magnesium Alloy Substrates Using Hydrothermal Methods. *Coatings* **2021**, *11*, 8. https://dx.doi.org/10.3390/coatings11010008

Received: 17 November 2020
Accepted: 22 December 2020
Published: 24 December 2020

1. Introduction

Magnesium and its alloys have been considered promising candidates for bone implants due to their unique biocompatibility and biodegradation [1]. As a biodegradable material, magnesium can be degraded in vivo and avoid the secondary implant removal surgery. This makes them more suitable materials for bone implants than the titanium alloys, stainless steel or other bioinert materials [2,3]. The degradation products of the Mg are mainly Mg^{2+} ions, which are essential for the human body [4]. The Young's modulus (E = 41–45 GPa) and density (1.74–1.84 g/cm^3) of magnesium are close or similar to those of the human bone (E = 15–25 GPa, density = 1.8–2.1 g/cm^3) [5,6]. Still, the application of biodegradable magnesium alloys has been restricted by their poor corrosion resistance, hence fast biodegradation [6]. Though the recommended daily intake for adults of magnesium is 240–420 mg/day, and the human body has a strong tolerance to magnesium ions [7], the rapid pH value increase and the hydrogen release during the degradation cause cell death and tissue inflammation [5,8]. Moreover, the rapid degradation of magnesium-based material would cause a sharp decrease in the mechanical strength of the implant, which might lead to the implantation failure [9].

Surface modification is an efficient method to improve the corrosion resistance of the magnesium alloys and delay its biodegradation. Polymer coatings [10–13] and ceramic coatings [8,14–16] have been successfully deposited on the magnesium alloys, showing great protection to the substrate [5,17,18]. Among numerous proposed coatings, hydroxyapatite ($Ca_{10}(PO_4)_6(OH)_2$, HA) is an efficient coating widely investigated because of its unique biocompatibility and great corrosion resistance [8,19,20]. Different techniques, such as micro-arc oxidation [21], electrophoretic deposition [22], laser treatment [23] and microwave-assisted (MW) processing [24], have been used to improve the corrosion resistance of the magnesium alloys. The hydrothermal method is one of the most popular methods that has been used to fabricate HA coatings on magnesium substrates [25]. This method has two main advantages: (1) The requirement for the equipment is relatively low [26], and (2) the HA coatings can be controlled by adjusting the paraments of the hydrothermal reactions [15,27].

The morphology and microstructure of the HA is crucial to the performance of the coatings [28]. The rod-like or plate-like HA coatings with different structures show significantly different performance as implants [29]. When using the hydrothermal methods, the parameters of the reaction would greatly affect the formation of HA coatings. For example, Xia [15] studied the effect of the Ca/P ratio, He [26] studied the influence of the addition of ethylenediaminetetraacetic acid (EDTA). Ion substitution has been widely used to adjust the morphology and the performance of the HA coatings [30–32]. Tomozawa [33] has proved that the pH of the precursor solution has a huge impact on the formation of the HA coatings, yet the degradation behavior and the biocompatibility of the different HA coatings had not been studied. To further improve the performance of the HA coatings, the formation mechanism and the corresponding degradation behavior of the HA coatings formed at different pH value requires further investigation.

In this paper, HA coatings are deposited on the ZK60 substrates using hydrothermal methods. By changing the pH value of the precursor solution, HA coatings with different morphology and microstructure are obtained. The formation mechanism of the HA crystals at different pH values, corrosion resistance and the biocompatibility of the HA coatings are investigated to identify the best HA coatings for a ZK60 magnesium alloy substrate.

2. Materials and Methods

2.1. Preparation of ZK60 Magnesium Alloy Substrates

A commercial ZK60 magnesium alloy plate (Mg, 4.8–6.2% Zn, Zr > 0.45%; Bo Gang Metal Materials Co., Ltd., Changsha, China) was cut into small squares of 10 mm × 10 mm × 1 mm with a DK70 EDM cutting machine. The pieces were polished up to a 2000 grit silicon carbide paper, and ultrasonically washed in alcohol for 10 min. Subsequently, the samples were washed in 90 vol.% phosphoric acid aqueous solution, and NaOH aqueous solution (1 mol/L) at 55 °C. The acid–alkaline washing procedure was repeated for several times until a smooth and bright surface was obtained. After rinsing in deionized (DI) water and alcohol, the ZK60 square-like samples were preserved in alcohol for further use.

2.2. Preparation of the HA Coatings

Preparation of HA coating was conducted according to procedure presented in [34]. Ethylenediaminetetraacetic acid disodium salt (EDTA-2Na), $Ca(NO_3)_2{\cdot}4H_2O$, and $NaH_2PO_4{\cdot}2H_2O$ chemical reagents (Sigma–Aldrich, Shanghai, China) of analytical grade were used without further purification. First, EDTA-2Na (0.01 mol/L) and $Ca(NO_3)_2{\cdot}4H_2O$ (0.03 mol/L) were dissolved in DI water and stirred for 30 min. Then, $NaH_2PO_4{\cdot}2H_2O$ was added in the precursor solution. After stirring 30 min, NaOH solution (3 mol/L) was slowly dropped into the solution to adjust the pH values of the precursor to 5, 7, and 9. The obtained solutions were filtered to remove the impurities and titrated to the marked volume with DI water.

The hydrothermal reactions were carried out in a stainless-steel autoclave with a 100 mL Teflon liner. The precursor solutions and the pre-treated substrates were transferred into the Teflon liner and placed in the autoclave. After the hydrothermal reactions at 120

°C for 2 h, the samples were rinsed with DI water three times and dried in air flow. The obtained samples are denoted as HA5, HA7, and HA9, according to the pH values of the precursor solutions.

2.3. Materials Characterization

The phase, morphology and structure of the coatings were identified and characterized by X-ray diffraction (XRD, CuKα radiation, Haoyuan DX-2700BH, Liaoning, Shanhai, China), field emission scanning electron microscopy (FE-SEM, Supra 40, Zeiss, Jena, Germany) equipped with EDS, and transmission electron microscopy (TEM, Hitachi H-800, Hitachi Ltd, Chiyoda, Japan). The current and the voltage of the X-ray tube were 30 mA and 30 kV, respectively. The cross-section images of the samples were obtained by polishing the samples fixed with epoxy resin. The samples immersed for 7 days were also fixed with epoxy resin to obtain the cross-section images.

2.4. Immersion Tests

Immersion tests were carried out to investigate the corrosion resistance and the degradation behavior of the samples in Hank's solution (Hank's balanced salts, H2387, Sigma–Aldrich, Shanghai, China) at 37 °C. The ratio of Hank's solution: Sample was 10 mL:1 g. ZK60 substrates polished to #2000 were used as control group. After a certain immersion time, the pH values of the soaked solution were measured using a pH-meter (PHSJ-6L, Leici, Shanghai, China).

2.5. Electrochemical Test

Electrochemical tests were carried out in Hank's using a Gamry electrochemical workstation (Gamry, Warminster, PA, USA) with a three-electrode system, with samples as the working electrode (10 $\times$ 10 mm^2 of exposed area), a platinum rod as the counter electrode, and a saturated calomel electrode (SCE) as the reference. The area exposed to Hank's solution was 1.0 cm^2. The change in the open-circuit potential (OCP) was first monitored as a function of immersion time for about 30 min. The scan frequency range was set from 10^5 to 10^{-2} Hz. The disturbance signal was a sinusoidal AC voltage with an amplitude of 5 mV, and the EIS data were fitted by ZSimpWin 3.10 software. The potential dynamic polarization experiments were conducted with a scan rate of 10 mV/s, from -2.0 to 0.0 V, and then the corrosion parameters were calculated using the Tafel extrapolation method.

2.6. Cell Culture Preparation

Four-week-old male Specific-Pathogen Free Sprague Dawley (SPF SD) rats were provided by the experimental animal center of Shanghai No.9 People's Hospital. The rats were sacrificed by neck dislocation, and bone marrow was obtained by rising the bone marrow cavity by Dulbecco's Modified Eagle's medium (DMEM) after cutting off the epiphysis at both ends of the femoral bones. The collected bone marrow washing fluid was centrifuged at 1800 rpm for 10 min. The cell suspension was seeded into the culture dish. The culture conditions were 37 °C, 5% CO_2, and the passage 2 to passage 4 of bone marrow mesenchymal stem cells (BMSC) were used in our research.

2.7. Cell Live/Dead Assay

After 24 h, the culture medium was removed and rinsed with phosphate buffered saline (PBS). The cells were stained with propidium iodide (PI) (1:1000 buffer) and Calcein-AM (1:1000 buffer) for 10 min and then photographed under a fluorescence microscope. The dead cells were stained with PI and the live cells were stained with Calcein-AM.

2.8. Statistical Analysis

Results were averaged and expressed as mean ± standard deviation. Statistical analysis was performed using analysis of variance (ANOVA). A value of $p < 0.05$ was considered statistically significant.

3. Results

3.1. Characterization of the HA Coatings

The obtained coatings were gently scraped off from the ZK60 magnesium substrates using a stainless-steel knife and characterized by XRD (Figure 1). The main phases of HA5 and HA7 coatings are Mg and HA, while the HA9 coating consists of HA and $Mg(OH)_2$. In addition, according to the intensity of the HA peaks, HA9 had higher crystallinity.

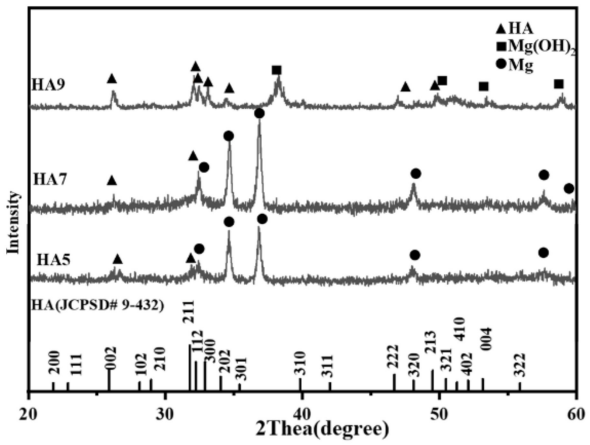

Figure 1. X-ray diffraction (XRD) patterns of hydroxyapatite (HA) coatings obtained at different pH values.

The scraped coatings were dispersed in ethyl alcohol and observed under the transmission electron microscope. Figure 2 shows the TEM images of the HA particles generated at different pH values. The aspect of HA5 and HA7 is flake-like, while HA9 is rod-like one, which is consistent with SEM images. For all samples, the SDAX patterns are identified as HA reflections. The rod structure of the HA9 shows that it has a preferential c-axis growth during the hydrothermal reaction.

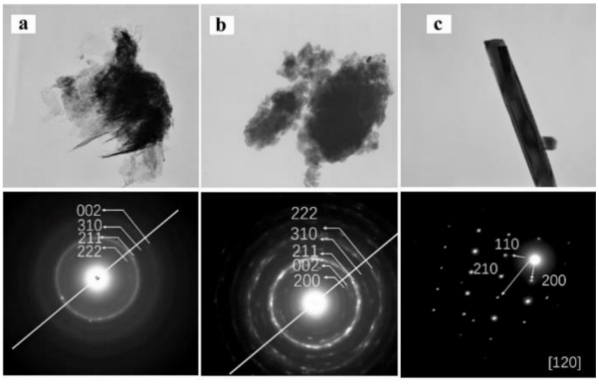

Figure 2. Transmission electron microscope (TEM) images and electron diffractions of HA5 (**a**), HA7 (**b**), and HA9 (**c**) particles.

Figure 3 displays the SEM images of coatings. They indicate that the pH value of the precursor solution has great impact on the coating morphologies. For the acid precursor solution, the HA5 exhibits a network structure composed of nanosheet HA, while the HA7

exhibits a nanoflower structure consisted of HA nanosheet. The size of HA5 nanosheet is larger than that of HA7. On the other hand, HA9 exhibits nanoflowers structure composed of HA nanorods. It is worth mentioning that other morphologies, than nanoflowers, attached on the substrate (Figure 3g), such as larger nanoflowers (Figure 3f). They can be found on the upper layer of HA9, but are not present on HA5 and HA7. It can be assumed that the larger nanoflowers formed in the solution, and later deposited on the substrate [15].

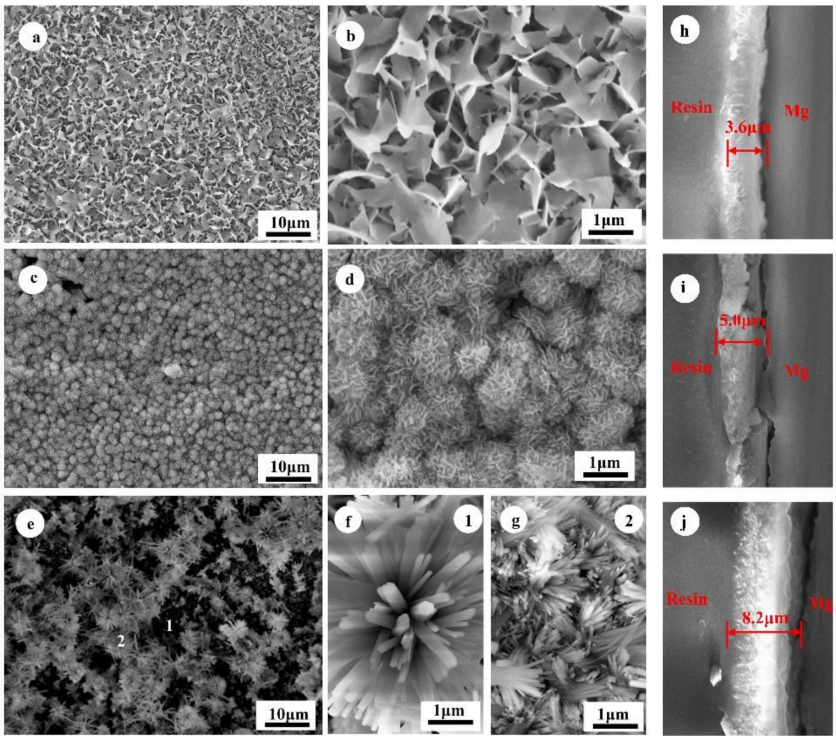

Figure 3. Scanning electron microscopy (SEM) images showing morphologies of HA5 (**a**,**b**), HA7 (**c**,**d**), and HA9 (**e**,**f**,**g**); cross-section images of the HA coatings, HA5 (**h**), HA7 (**i**), and HA9 (**j**).

The thickness of the coatings was measured by the cross-section images. The thicknesses of the HA5, HA7, and HA9 were 3.6, 5.0, and 8.2 μm, respectively. The high pH value of the precursor solution ensured the formation of the hydroxyapatite crystals [33] and the HA9 coatings were the thickest among these three coatings.

3.2. Wettability of HA Coatings

Wettability can influence the protein absorption and cell attachment [35]. Studies have shown that hydrophilic surfaces can promote osteoblastic cell growth and mineral deposition [29]. The wettability of the samples was characterized according to their contact angles by sessile drops of water on the coating surfaces. Figure 4 indicates that the ZK60 substrate is hydrophilic, because its contact angle is ~70°. On the other hand, the HA-coated samples have improved hydrophilic surfaces, since their contact angles are all much lower than 70°. In general, the wettability of the coatings depends on the chemical components, morphologies and crystallinities [29]. It was reported that pure HA exhibits the hydrophilicity with a contact angle of about 24.8° [36]. The HA7 sample (Figure 4c) shows a similar contact angle as pristine HA, since its main component is HA, and HA5 (Figure 4b) shows a lower contact angle. However, HA5 has a lower crystallinity, because Ca^{2+} and PO_4^{3-} ions, with good ion activity, lead to higher wettability, exhibited by a smaller contact angle of HA5 than HA7. The HA9 has the smallest contact angle, 7.7°, hence the greatest hydrophilicity. The smallest contact angle of HA9 might be caused

by the existence of the $Mg(OH)_2$, considering that the presence of abundant OH^- ions improves the hydrophilicity [35].

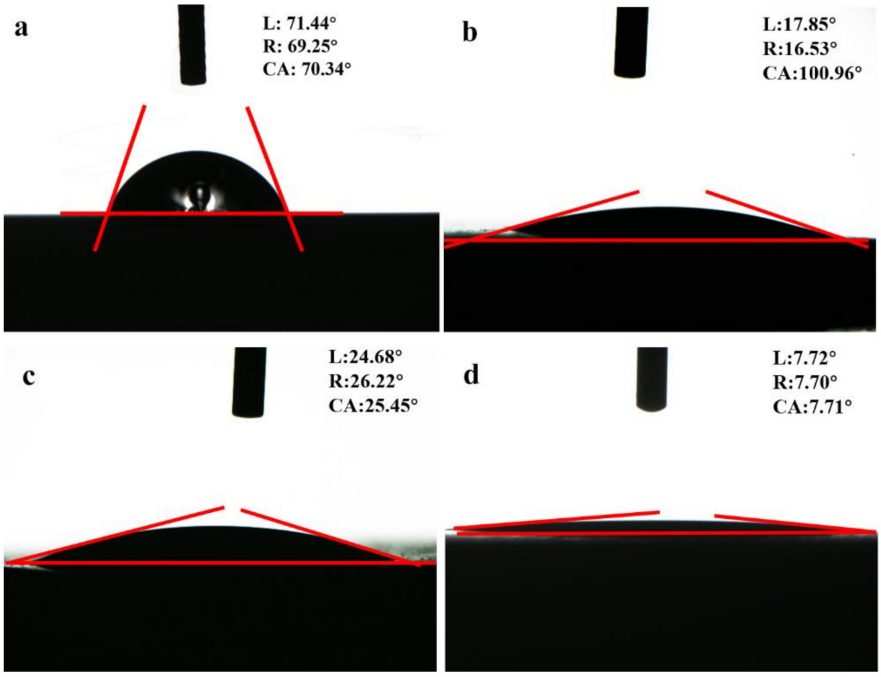

Figure 4. Contact angle measurement of Hank's solution on the surface of samples, ZK60 (**a**), HA5 (**b**), HA7 (**c**), and HA9 (**d**).

3.3. Electrochemical Tests of the HA-Coated Samples

Figure 5 displays the Tafel plots of ZK60 and HA-coated samples. The cathodic polarization curve represents the cathodic hydrogen evolution, while the anodic polarization curve represents the dissolution of Mg [37]. HA coatings enhance the corrosion resistance of the ZK60 substrate, as can been seen from the decrease I_{corr} (Table 1). The I_{corr} values of HA5 and HA7 are lower than that of the HA9. The presence of $Mg(OH)_2$ might affect the HA9 corrosion resistance, as it may cause a poor adherence of HA coating.

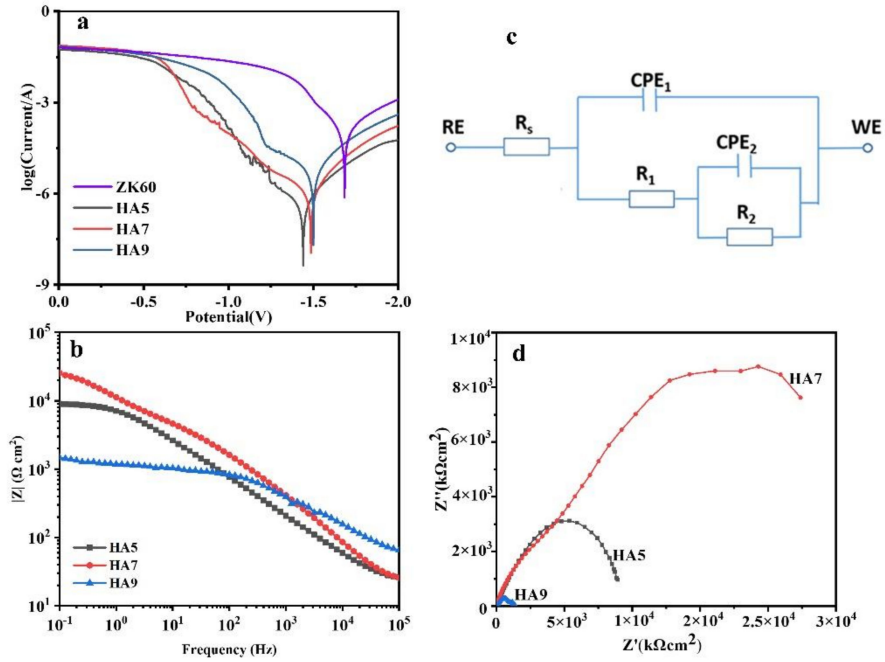

Figure 5. (**a**) Polarization curves of the ZK60 substrate and the HA-coated samples. (**b**) Equivalent circuits used to fit the impedance data for uncoated and coated ZK60 magnesium alloy samples. Bode (**c**) and Nyquist (**d**) plots of the HA-coated samples.

Table 1. Corrosion potential and current density of the ZK60 and HA-coated samples in Hank's solution.

Sample	I_{corr} ($A \cdot cm^{-2}$)	E_{corr} (V)
ZK60	$1.46 \cdot 10^{-4}$	−1.68
HA5	$5.28 \cdot 10^{-7}$	−1.44
HA7	$1.04 \cdot 10^{-6}$	−1.49
HA9	$5.09 \cdot 10^{-6}$	−1.50

Figure 5c,d is the Bode and Nyquist plots of the HA-coated samples. The diameter of the capacitive semicircle of measured Nyquist spectrum is closely related to the corrosion rate [38]. HA7 has the largest dimension of capacitive, followed by HA5 and HA9, showing that HA7 has the best corrosion resistance.

The degradation behavior of the HA-coated samples was analyzed through EIS spectra. The EIS results were calculated using the equivalent circuits shown in Figure 5b, where Rs represents the resistance of SBF solution, R_1 represents the resistance of the outer loose layer, CPE_1 represents the capacitance of the solution/outer film interface, CPE_2 represents the capacitance of the inner film/ matrix interface, R_2 represents the charge transfer resistance, and n is the power index. The calculated results using this equivalent circuit diagram are shown in Table 2. For all three samples, R_1 and R_2 are much larger than R_s, indicating that the R_1 and R_2 play a major role in the impedance of the sample. The R_1 value of the HA5 is smaller than that of the HA7, since the HA layer of HA5 is thinner. The R_1 value of the HA9 is even much smaller than that of the HA5, which can be attributed to the presence of $Mg(OH)_2$. The R_2 value of the HA5 and HA7 is much larger than that of HA9, indicating that the HA5 and HA7 have more compact interface combination with the substrate and HA5 is firmly attached to the substrate. In addition, HA7 has the largest total impedance ($R_1 + R_2 + R_s$), showing that the HA7 coating can offer better protection.

Table 2. Fitting results of EIS plots for ZK60 and HA-coated samples, in Hank's solution.

Sample	R_s ($\Omega \cdot cm^2$)	$(CPE\text{-}T)_1$ ($S^{-n} \cdot cm^{-2}$)	R_1 ($\Omega \cdot cm^2$)	$(CPE\text{-}T)_2$ ($S^{-n} \cdot cm^{-2}$)	R_2 ($\Omega \cdot cm^2$)
HA5	36.25	$5.14 \cdot 10^{-5}$	$6.17 \cdot 10^{2}$	$4.26 \cdot 10^{-6}$	$7.14 \cdot 10^{3}$
HA7	32.90	$2.65 \cdot 10^{-7}$	$2.69 \cdot 10^{3}$	$6.39 \cdot 10^{-6}$	$1.76 \cdot 10^{3}$
HA9	62.51	$9.74 \cdot 10^{-10}$	$2.64 \cdot 10^{2}$	$8.53 \cdot 10^{-7}$	$7.36 \cdot 10^{2}$

3.4. Immersion Tests

Immersion tests were conducted for further study of the corrosion behavior of the samples. Figure 6 presents the variation of pH value of Hanks' solution during the immersion tests. The increase of pH value results from the release of OH^- concentration caused by the degradation of Mg [3]. For the uncoated ZK60 substrates, Mg would rapidly dissolve and lead to the local alkalization [1]. Therefore, as shown in Figure 6, after three days, the pH value of the soaking solution of naked ZK60 sharply exceeded eight units. Comparing to the uncoated ZK60 substrate, in the initial stage of the immersion, the HA-coated samples show moderate pH value increase, due to the protective HA coatings. HA7 and HA5 show an improved protection than HA9. After seven days of immersion, the pH value of the solution containing HA7 stabilized at around 8, while the HA9 reached 10 units. The pH variation confirms that HA7 and HA5 coatings greatly enhance the corrosion resistance, while HA9 coating provides limited protection to the substrate.

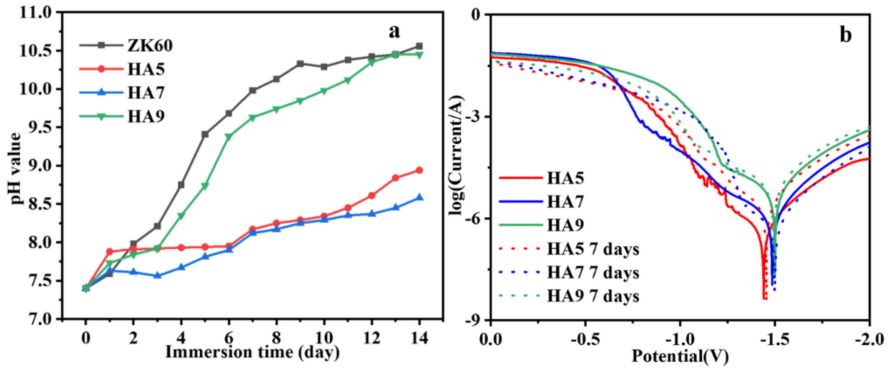

Figure 6. (**a**) Variation of pH of Hank's solution containing immersed sample. (**b**) Polarization curves of the immersed HA samples.

After seven days' immersion, the samples were taken out and conducted with the electrochemical test in SBF. Polarization curves of HA samples immersion (Figure 6b) show that, after being immersed in SBF for seven days, the E_{corr} and I_{corr} of HA5 and HA7 barely changed, while I_{corr} and E_{corr} of HA9 largely increased (Table 3). This indicates that HA9 has a deteriorated corrosion resistance after the immersion, while HA5 and HA7 preserved their high corrosion resistance.

Table 3. Calculated corrosion potential and current density of the soaked samples.

Soaked Samples	I_{corr} ($A \cdot cm^{-2}$)	E_{corr} (V)
HA5	1.44	1.45
HA7	1.49	1.49
HA9	1.50	1.49

The optical images of the immersed samples (Figure 7) shows areas where HA coating has been peeled off from the substrate. However, the HA coatings of HA5 and HA7 almost remained unaffected after seven days of immersion, and the layer can still protect the

substrate from the corrosion activity, which should explain the difference between the soaked HA5, HA7, and HA9 samples.

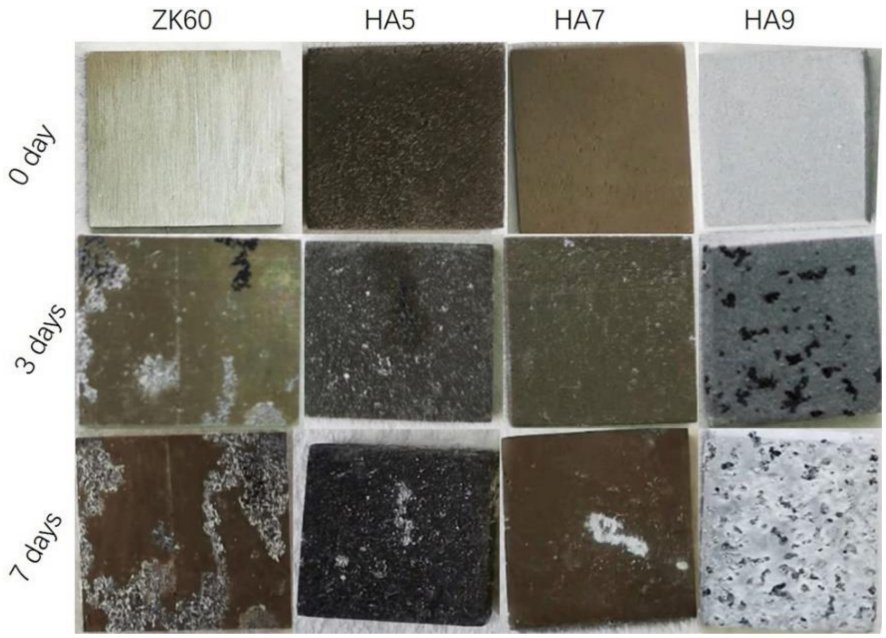

Figure 7. Optical images of the immersed samples.

The SEM images of the morphology of the immersed samples are represented in Figure 8. After seven days of immersion, cracks on the substrates can be observed, indicating that all the samples have been corroded. For the HA9, most of the HA nanoflowers have peeled off from the substrate and part of the Mg substrate was exposed to the corrosion medium, which consists with the optical images of the immersed samples. The network structure of the HA5 vanished, and particles remained on the surface. Similarly, the initial nanoflower-like HA can be no longer observed, and spherical particles can be observed instead. The morphological changes of the HA5 and HA7 during the immersion tests can be attributed to deposited CaP or $Mg(OH)_2$ [39]. However, the existence of the layers of the HA5 and HA7 were still dense and could insulate the substrate from the corrosion medium. Therefore, the high corrosion resistance of HA7 and HA5 can be preserved after the immersion, while protection of the HA coatings generated in alkaline environment is poor for long-term immersion conditions. In addition, as can be seen from the cross-section images, the HA9 has been serious corroded and corrosion pits can be observed (Figure 8i). On the other hand, the integrate interface of HA5 and HA7 (Figure 8h,i) confirmed their great corrosion resistance.

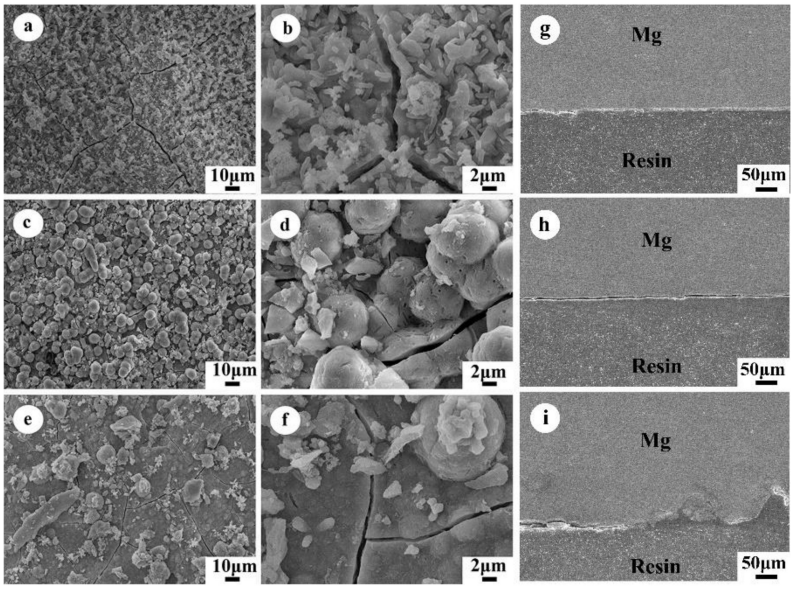

Figure 8. SEM images of HA5 (**a**,**b**), HA7 (**c**,**d**), and HA9 (**e**,**f**); and cross-section SEM images of HA5 (**g**), HA7 (**h**), and HA9 (**i**) after being soaked in Hank's solution for seven days.

3.5. Cell Culture of BMSCs

Figure 9 shows the cell viabilities of the BMSCs after 24 h culture. The BMSCs on the ZK60 substrate show low cell viability, because of high alkalization induced by the rapid degradation of the magnesium [8]. Statistical results of percentage of live cells show that the HA coatings can improve the cell viability, and HA7 has the highest cell viability. Many researches have shown that the cell viability is related to the local pH value, as high pH value leads to cell death [40]. Thus, HA coating can mitigate the degradation of magnesium and prevent high local alkalization, hence improving the cell viability. Therefore, the general trend of the cell viability (Figure 9) is consistent with the trend of the corrosion resistance.

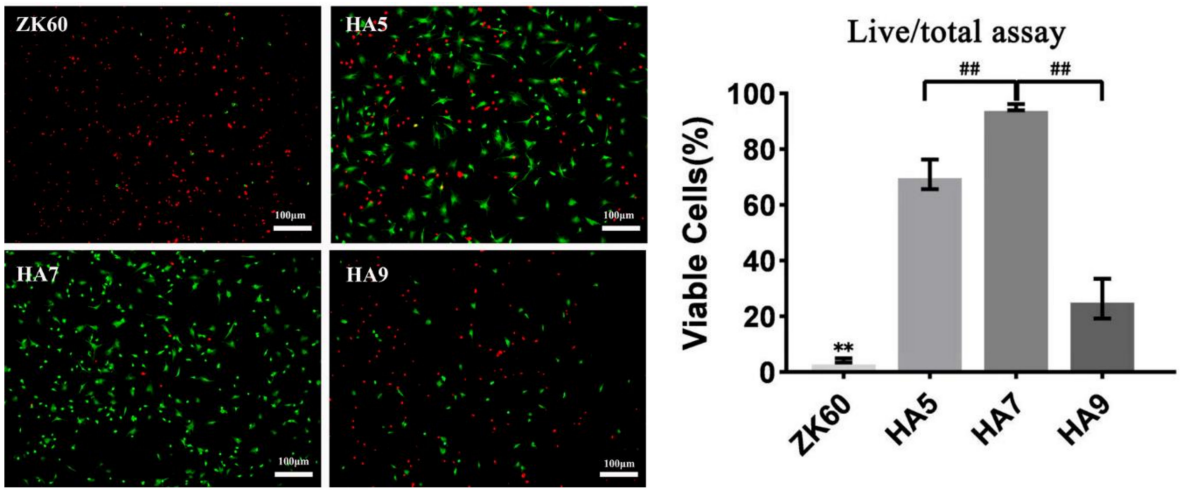

Figure 9. Fluorescence images of the bone marrow stem cells (BMSCs) and the statistical results of percentage of live cells after 24 h culture. (** represents $p < 0.01$ compared with other groups ## represents $p < 0.01$).

4. Discussion

In this paper, HA coatings were successfully prepared on ZK60 magnesium alloys using hydrothermal methods. Both the XRD patterns and the electron diffraction in TEM have proved that HA coating can be fabricated on the ZK60 magnesium alloys. The formation of the HA can be schematically explained, as described in Figure 10. The hydrothermal reaction starts with the dissolution of the Mg [15]:

$$Mg \rightarrow Mg^{2+} + 2e^{-} \quad (1)$$

$$2H_2O + 2e^{-} \rightarrow 2OH^{-} + H_2 \quad (2)$$

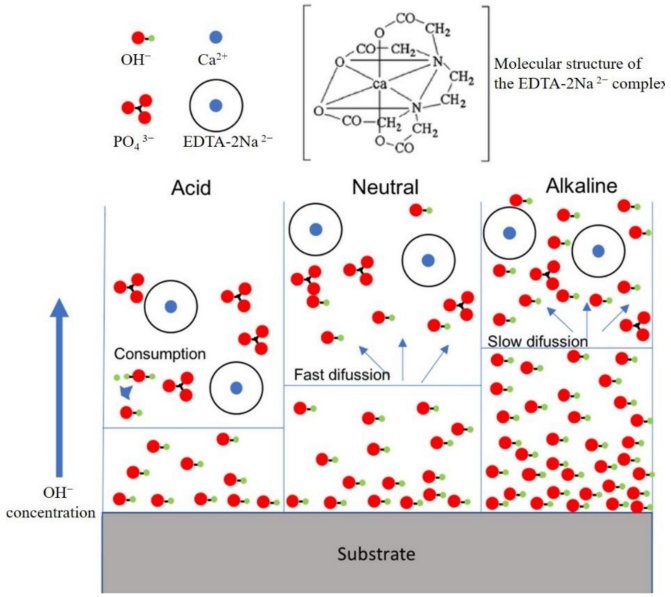

Figure 10. Diagram of the hydrothermal reaction at different pH values.

In the initial stage of the hydrothermal reaction, Mg^{2+} ions and OH^- ions would be produced nearby the surface of the substrate. The generated OH^- ions could react with the $H_2PO_4^-$ and Ca^{2+} ions according to the following Equations [41]:

$$Ca^{2+} + H_2PO_4^- + OH^- + H_2O \rightarrow CaHPO_4 \cdot 2H_2O \quad (3)$$

$$10CaHPO_4 + 12OH^- \rightarrow Ca_{10}(PO_4)_6(OH)_2 + 4PO_4^{3-} + 10H_2O \quad (4)$$

In addition, the abundant OH^- ions would react with the released Mg^{2+} ions, according to the following Equation [20]:

$$Mg^{2+} + 2OH^- \rightarrow Mg(OH)_2 \quad (5)$$

As described in Figure 10, according to Equations (3) and (4), the formation of hydroxyapatite also requires OH^- ions. When the local environment is acid, abundant OH^- ions would be generated around the surface, since the magnesium would dissolve and generate OH^- ions. Part of the OH^- ions reacts with the H^+ ions from the precursor solution, and the OH^- concentration away from the substrate is too low to promote the reactions (3) and (4). The diffraction peaks of the three crystal planes of HA, (211), (112), and (300) are quite sharp in the XRD patterns of HA9, showing the higher crystallinity of HA comparing with the HA5 and HA7 [26]. Moreover, the abundant OH^- ions could react with the Mg^{2+} ions and form $Mg(OH)_2$ (Equation (5)) [20], which can be found in the XRD patterns of the HA9.

It is worth mentioning that Mg peaks are not found in the XRD pattern of HA9 but appeared in the XRD patterns of the HA5 and HA7 (Figure 1). Since the HA coatings were softly scraped from the substrates, the Mg peaks should not be contributed to the substrate. For HA5 and HA7, the formation of hydroxyapatite would only occur around the surface, and the in-situ HA crystals grow on the substrate surface and show strong adhesion, leading to the simultaneous peeling of Mg fragments and HA crystals. On the other hand, in the alkaline environment, the HA crystals could form in the precursor solution, followed by precipitation on the substrate, hence a relatively low adhesion.

These differences lead to huge differences in HA corrosion resistance and degradation. First of all, there is a large amount of $Mg(OH)_2$ in the HA9 coating, which also leads to the looseness of the HA9 coating. At the same time, due to the weak bonding force between HA9 and the substrate, the protection of the base by HA9 is limited. It can also be seen from impedance spectroscopy and immersion experiments that HA9 has poor corrosion resistance. More importantly, the coating of HA9 will fall off during the immersion process, which causes the protection of the substrate to gradually disappear after immersion. On the other hand, HA5 and HA7 have better adhesion to the substrate, so they also have better corrosion resistance. It is worth mentioning that HA7 has a fuller flower-like structure than HA5, which may be due to the fact that HA is easier to crystallize under neutral conditions than under acidic conditions. This also makes HA7 have better corrosion resistance than HA5. The excellent corrosion resistance of HA coating ultimately determines its biocompatibility.

In addition, the HA coatings show different morphology and microstructure under different local pH value. Figure 11 briefly illustrates the formation mechanism of the HA morphologies, assuming the initial single HA crystal is formed, and the HA crystal can grow along the a(b)-plane or c-axis [26]. Apparently, the initial growth along the a(b)-plane requires the $Ca\text{-}PO_3$ units, while the initial growth along the c-axis requires the $Ca\text{-}PO_3$ and $Ca\text{-}OH^-$ units at the same time. Since the OH^- ion concentration is relatively low in the acid and neutral environments, the HA crystal growth along the c-axis will be depressed and have a preferential growth along the a(b)-plane. This growth pattern will finally lead to the formation of nanoflake-like HA in the acid and neutral environments [26]. On the other hand, when the precursor solution is alkaline, the OH^- ions are abundant, and the nanorod-like HA will have the preferential c-axis growth [29], leading to formation of nanorod crystals. The growth along c axis shows a circular distribution because of the screw dislocation growth pattern [20].

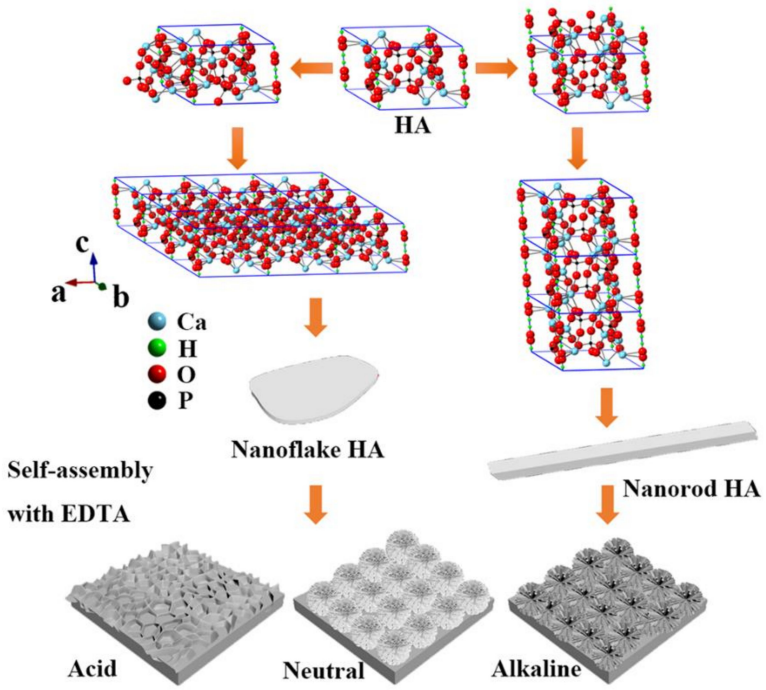

Figure 11. Diagram of the formation mechanism of different HA morphologies.

At the same time, EDTA was a chelating agent that has strong chelation to certain metal ions and ion selectivity [42]. Usually, the existence of EDTA-2Na would lead to a nanoflower [26] or network morphology [20]. However, since only the area near the surface has the sufficient OH^- ion concentration to allow the formation of the HA, the HA can only be generated nearby surface and the HA crystals can only distribute around the surface, forming a thin network structure attached on the surface (Figure 3a,b). On the other hand, as shown in Figure 5, when the area that could allow the formation of the HA is not restricted around the surface, the flower-like HA morphology will form, as it can be observed for HA7 and HA9 samples.

The different growing pattern leads to different degradation behavior and performance of HA coatings. Immersion and electrochemical tests show that the neutral environment promote formation of HA coatings with high corrosion resistance. The cell culture experiments confirm that the enhanced corrosion resistance assure the biocompatibility of the substrate-coating system. In general, the HA coating prepared in neutral environment shows great potential in surface modification of magnesium alloys.

5. Conclusions

In this paper, HA coatings were successfully deposited on the ZK60 magnesium substrates using hydrothermal methods. By adjusting the pH value of the precursor solution, the morphology and microstructure of the HA coatings evolved and greatly affected the performance of coatings. Other than the morphology evolution, in acid and neutral environment, HA showed lower crystallinity but firm attachment to the substrate. On the other hand, the alkaline environment improves the crystallinity, but the HA tends to be generated in the precursor solution and later precipitates on the substrate, in which case the adhesion to the substrate would be relatively low. As a result, HA5 and HA7 coatings retained on the substrate and HA9 tends to peel off during the immersion. In addition, the flake-HA also promotes the precipitation of CaP, resulting in the long-term protection to the substrate. The results indicate that the pH value of the precursor solution is an important factor to obtain and deposit enhanced HA coatings on the magnesium substrates. The HA coating obtained in the neutral precursor solution has high corrosion

resistance and ideal degradation behavior, showing great potential in surface modification of magnesium alloys.

Author Contributions: Conceptualization, T.W. and W.L.; methodology, T.W.; validation, T.W. and W.L.; formal analysis, T.W.; investigation, T.W.; resources, T.W., C.L., and J.H.; data curation, T.W. and C.L.; writing—original draft preparation, T.W.; writing—review and editing, D.B.; visualization, T.W.; supervision, W.L. project administration, W.L.; funding acquisition, W.L. All authors have read and agreed to the published version of the manuscript.

Funding: The present work was funded by National Natural Science Foundation of China (Grant No. 51471120).

Institutional Review Board Statement: Four-week-old male Specific-Pathogen Free Sprague Dawley (SPF SD) rats were provided by the experimental animal center of Shanghai No.9 People's Hospital. The rats were sacrificed by neck dislocation, and bone marrow was obtained by rising the bone marrow cavity by Dulbecco's Modified Eagle's medium (DMEM) after cutting off the epiphysis at both ends of the femoral bones. These procedures were conducted by Master Chao Lin.

Informed Consent Statement: Not applicable.

Data Availability Statement: The data presented in this study are available on request from the corresponding author.

Conflicts of Interest: The authors declare no conflict of interest.

References

1. Sanchez, A.H.M.; Luthringer, B.J.; Feyerabend, F.; Willumeit, R. Mg and Mg alloys: How Comparable are In Vitro and In Vivo Corrosion Rates? A Review. *Acta Biomater.* **2015**, *13*, 16–31. [CrossRef] [PubMed]
2. Zheng, Y.; Gu, X.; Witte, F. Biodegradable metals. *Mater. Sci. Eng. R Rep.* **2014**, *77*, 1–34. [CrossRef]
3. Liu, C.; Ren, Z.; Xu, Y.; Pang, S.; Zhao, X.; Zhao, Y. Biodegradable Magnesium Alloys Developed as Bone Repair Materials: A Review. *Scanning* **2018**, *2018*, 9216314. [CrossRef] [PubMed]
4. Li, L.; Zhang, M.; Li, Y.; Zhao, J.; Qin, L.; Lai, Y. Corrosion and biocompatibility improvement of magnesium-based alloys as bone implant materials: A review. *Regen. Biomater.* **2017**, *4*, 129–137. [CrossRef]
5. Agarwal, S.; Curtin, J.; Duffy, B.; Jaiswal, S. Biodegradable magnesium alloys for orthopaedic applications: A review on corrosion, biocompatibility and surface modifications. *Mater. Sci. Eng. C Mater. Biol. Appl.* **2016**, *68*, 948–963. [CrossRef]
6. Gu, X.; Li, S.-S.; Li, X.-M.; Fan, Y.-B. Magnesium based degradable biomaterials: A review. *Front. Mater. Sci.* **2014**, *8*, 200–218. [CrossRef]
7. Trumbo, P.; Schlicker, S.; Yates, A.A.; Poos, M. Dietary Reference Intakes for Energy, Carbohydrate, Fiber, Fat, Fatty Acids, Cholesterol, Protein and Amino Acids. *J. Am. Diet. Assoc.* **2002**, *102*, 1621–1630. [CrossRef]
8. Husak, Y.; Solodovnik, A.; Yanovska, A.; Kozik, Y.; Liubchak, I.; Ivchenko, V.; Mishchenko, O.; Zinchenko, Y.; Kuznetsov, V.; Pogorielov, M. Degradation and In Vivo Response of Hydroxyapatite-Coated Mg Alloy. *Coatings* **2018**, *8*, 375. [CrossRef]
9. Özarslan, S.; Şevik, H.; Sorar, I. Microstructure, mechanical and corrosion properties of novel Mg-Sn-Ce alloys produced by high pressure die casting. *Mater. Sci. Eng. C Mater. Biol. Appl.* **2019**, *105*, 110064. [CrossRef]
10. Li, L.-Y.; Cui, L.-Y.; Zeng, R.-C.; Li, S.-Q.; Chen, X.-B.; Zheng, Y.; Kannan, M.B. Advances in functionalized polymer coatings on biodegradable magnesium alloys—A review. *Acta Biomater.* **2018**, *79*, 23–36. [CrossRef]
11. Wei, Z.; Tian, P.; Liu, X.; Zhou, B. Hemocompatibility and selective cell fate of polydopamine-assisted heparinized PEO/PLLA composite coating on biodegradable AZ31 alloy. *Colloids Surf. B Biointerfaces* **2014**, *121*, 451–460. [CrossRef] [PubMed]
12. Yuan, M.; Xiong, C.; Jiang, L.; Li, H.; Yuan, M. The Preparation, Characterization, Mechanical and Antibacterial Properties of GO-ZnO Nanocomposites with a Poly(l-lactide)-Modified Surface. *Materials* **2018**, *11*, 323. [CrossRef] [PubMed]
13. Kang, Y.; Wang, C.; Shi, X.; Zhang, G.; Chen, P.; Wang, J. Crystallization, rheology behavior, and antibacterial ap-plication of graphene oxide-graft-poly(l-lactide)/poly (l-lactide) nanocomposites. *Appl. Surf. Sci.* **2018**, *451*, 315–324. [CrossRef]
14. Mukhametkaliyev, T.M.; Surmeneva, M.A.; Vladescu, A.; Cotrut, C.M.; Braic, M.; Dinu, M.; Vranceanu, D.M.; Pana, I.; Mueller, M.; Surmenev, R.A. A biodegradable AZ91 magnesium alloy coated with a thin nanostructured hydroxyapatite for improving the corrosion resistance. *Mater. Sci. Eng. C* **2017**, *75*, 95–103. [CrossRef]
15. Xia, K.; Pan, H.; Wang, T.; Ma, S.; Niu, J.; Xiang, Z.; Song, Y.; Yang, H.; Tang, X.; Lu, W. Effect of Ca/P ratio on the structural and corrosion properties of biomimetic CaP coatings on ZK60 magnesium alloy. *Mater. Sci. Eng. C* **2017**, *72*, 676–681. [CrossRef] [PubMed]
16. Feng, Y.; Ma, X.; Chang, L.; Zhu, S.; Guan, S. Characterization and cytocompatibility of polydopamine on MAO-HA coating supported on Mg-Zn-Ca alloy. *Surf. Interface Anal.* **2017**, *49*, 1115–1123. [CrossRef]
17. Khalajabadi, S.Z.; Abu, A.B.H.; Ahmad, N.; Yajid, M.A.M.; Hj Redzuan, N.B.; Nasiri, R.; Haider, W.; Noshadi, I. Bio-corrosion behavior and mechanical characteristics of magnesium-titania-hydroxyapatite nanocomposites coated by magnesi-um-oxide flakes and silicon for use as resorbable bone fixation material. *J. Mech. Behav. Biomed. Mater.* **2018**, *77*, 360–374. [CrossRef]

18. Su, Y.; Li, D.; Su, Y.; Lu, C.; Niu, L.; Lian, J.; Li, G. Improvement of the Biodegradation Property and Biomineraliza-tion Ability of Magnesium–Hydroxyapatite Composites with Dicalcium Phosphate Dihydrate and Hydroxyapatite Coatings. *ACS Biomater. Sci. Eng.* **2016**, *2*, 818–828. [CrossRef]
19. Perez, J.R.; Kouroupis, D.; Li, D.J.; Best, T.M.; Kaplan, L.; Correa, D. Tissue Engineering and Cell-Based Therapies for Fractures and Bone Defects. *Front. Bioeng. Biotechnol.* **2018**, *6*, 105. [CrossRef]
20. Fan, X.-L.; Huo, Y.-F.; Li, C.-Y.; Kannan, M.B.; Chen, X.-B.; Guan, S.-K.; Zeng, R.-C.; Ma, Q.-L. Corrosion resistance of nanostructured magnesium hydroxide coating on magnesium alloy AZ31: Influence of EDTA. *Rare Met.* **2019**, *38*, 520–531. [CrossRef]
21. Dou, J.; Chen, Y.; Yu, H.; Chen, C. Research status of magnesium alloys by micro-arc oxidation: A review. *Surf. Eng.* **2017**, *33*, 731–738. [CrossRef]
22. Zhuang, J.J.; Song, R.; Xiang, N.; Xiong, Y.; Hu, Q. Effect of current density on microstructure and properties of PEO ceramic coatings on magnesium alloy. *Surf. Eng.* **2016**, *33*, 744–752. [CrossRef]
23. Mehrjou, B.; Soltani, R.; Sohi, M.H.; Torkamany, M.J.; Valefi, Z.; Ghorbani, H. Laser surface treatment of AZ91 magnesium alloy presprayed with WC–Co. *Surf. Eng.* **2016**, *32*, 893–901. [CrossRef]
24. Hassan, M.N.; Mahmoud, M.M.; El-Fattah, A.A.; Kandil, S. Microwave-assisted preparation of Nano-hydroxyapatite for bone substitutes. *Ceram. Int.* **2016**, *42*, 3725–3744. [CrossRef]
25. Sun, R.X.; Liu, P.; Zhang, R.X.; Lv, Y.P.; Chen, K.Z. Hydrothermal synthesis of microstructured fluoridated hydrox-yapatite coating on magnesium alloy. *Surf. Eng.* **2016**, *32*, 879–884. [CrossRef]
26. He, D.; Du, J.; Liu, P.; Liu, X.; Chen, X.; Li, W.; Zhang, K.; Ma, F. Influence of EDTA-2Na on the hydroxyapatite coating deposited by hydrothermal-electrochemical method on Ti6Al4V surface. *Surf. Coat. Technol.* **2019**, *365*, 242–247. [CrossRef]
27. Yu, W.; Sun, R.; Guo, Z.; Wang, Z.; He, Y.; Lu, G.; Chen, P.; Chen, K. Novel fluoridated hydroxyapatite/MAO composite coating on AZ31B magnesium alloy for biomedical application. *Appl. Surf. Sci.* **2019**, *464*, 708–715. [CrossRef]
28. Zhou, W.; Hu, Z.; Wang, T.; Yang, G.; Xi, W.; Gan, Y.; Lu, W.; Hu, J. Enhanced corrosion resistance and bioactivity of Mg alloy modified by Zn-doped nanowhisker hydroxyapatite coatings. *Colloids Surf. B Biointerfaces* **2020**, *186*, 110710. [CrossRef]
29. Chen, W.; Tian, B.; Lei, Y.; Ke, Q.-F.; Zhu, Z.; Guo, Y.-P. Hydroxyapatite coatings with oriented nanoplate and nanorod arrays: Fabrication, morphology, cytocompatibility and osteogenic differentiation. *Mater. Sci. Eng. C* **2016**, *67*, 395–408. [CrossRef]
30. Gokcekaya, O.; Ueda, K.; Narushima, T.; Ergun, C. Synthesis and characterization of Ag-containing calcium phosphates with various Ca/P ratios. *Mater. Sci. Eng. C* **2015**, *53*, 111–119. [CrossRef]
31. Gokcekaya, O.; Webster, T.J.; Ueda, K.; Narushima, T.; Ergun, C. In vitro performance of Ag-incorporated hydroxy-apatite and its adhesive porous coatings deposited by electrostatic spraying. *Mater. Sci. Eng. C* **2017**, *77*, 556–564. [CrossRef] [PubMed]
32. Gokcekaya, O.; Ueda, K.; Ogasawara, K.; Kanetaka, H.; Narushima, T. In vitro evaluation of Ag-containing calcium phosphates: Effectiveness of Ag-incorporated beta-tricalcium phosphate. *Mater. Sci. Eng. C Mater. Biol. Appl.* **2017**, *75*, 926–933. [CrossRef] [PubMed]
33. Tomozawa, M.; Hiromoto, S. Microstructure of hydroxyapatite- and octacalcium phosphate-coatings formed on magnesium by a hydrothermal treatment at various pH values. *Acta Mater.* **2011**, *59*, 355–363. [CrossRef]
34. Chen, J.; Tan, L.; Yang, K. Recent advances on the development of biodegradable magnesium alloys: A review. *Mater. Technol.* **2016**, *31*, 681–688. [CrossRef]
35. Surmeneva, M.A.; Kleinhans, C.; Vacun, G.; Kluger, P.J.; Schönhaar, V.; Müller, M.; Hein, S.B.; Wittmar, A.; Ulbricht, M.; Prymak, O.; et al. Nano-hydroxyapatite-coated metal-ceramic composite of iron-tricalcium phosphate: Improving the surface wettability, adhesion and proliferation of mesenchymal stem cells in vitro. *Colloids Surf. B Biointerfaces* **2015**, *135*, 386–393. [CrossRef]
36. Qu, H.; Wei, M. The effect of fluoride contents in fluoridated hydroxyapatite on osteoblast behavior. *Acta Biomater.* **2006**, *2*, 113–119. [CrossRef]
37. Zhao, Y.-B.; Liu, H.-P.; Li, C.-Y.; Chen, Y.; Zeng, R.-C.; Zeng, R.-C.; Wang, Z.-L. Corrosion resistance and adhesion strength of a spin-assisted layer-by-layer assembled coating on AZ31 magnesium alloy. *Appl. Surf. Sci.* **2018**, *434*, 787–795. [CrossRef]
38. Chen, J.; Tan, L.; Yang, K. Effect of heat treatment on mechanical and biodegradable properties of an extruded ZK60 alloy. *Bioact. Mater.* **2017**, *2*, 19–26. [CrossRef]
39. Shrestha, S. Magnesium and surface engineering. *Surf. Eng.* **2010**, *26*, 313–316. [CrossRef]
40. Yang, H.; Xia, K.; Wang, T.; Niu, J.; Song, Y.; Xiong, Z.; Zheng, K.; Wei, S.; Lu, W. Growth, in vitro biodegradation and cytocompatibility properties of nano-hydroxyapatite coatings on biodegradable magnesium alloys. *J. Alloy. Compd.* **2016**, *672*, 366–373. [CrossRef]
41. Wang, X.; Shi, J.; Li, Z.; Zhang, S.; Wu, H.; Jiang, Z.; Yang, C.; Tian, C. Facile one-pot preparation of chi-tosan/calcium pyrophosphate hybrid microflowers. *ACS Appl. Mater. Interfaces* **2014**, *6*, 14522–14532. [CrossRef] [PubMed]
42. Huang, H.; Liu, L.; Zhang, L.; Zhao, Q.; Zhou, Y.; Yuan, S.; Tang, Z.; Liu, X. Peroxidase-Like Activity of Ethylene Diamine Tetraacetic Acid and Its Application for Ultrasensitive Detection of Tumor Biomarkers and Circular Tumor Cells. *Anal. Chem.* **2016**, *89*, 666–672. [CrossRef] [PubMed]